Ocean Modelling 126 (2018) 63–76

Contents lists available at ScienceDirect

Ocean Modelling

journal homepage: www.elsevier.com/locate/ocemod

On the upper ocean turbulent dissipation rate due to microscale breakers and small whitecaps

Michael L. Banner*, Russel P. Morison

School of Mathematics and Statistics, The University of New South Wales, Sydney 2052, Australia

A B S T R A C T

In ocean wave modelling, accurately computing the evolution of the wind-wave spectrum depends on the source terms and the spectral bandwidth used. The wave dissipation rate source term which spectrally quantifies wave breaking and other dissipative processes remains poorly understood, including the spectral bandwidth needed to capture the essential model physics. The observational study of Sutherland and Melville (2015a) investigated the relative dissipation rate contributions of breaking waves, from large-scale whitecaps to microbreakers. They concluded that a large fraction of wave energy was dissipated by microbreakers. However, in strong contrast with their findings, our analysis of their data and other recent data sets shows that for young seas, microbreakers and small whitecaps contribute only a small fraction of the total breaking wave dissipation rate. For older seas, we find microbreakers and small whitecaps contribute a large fraction of the *breaking wave* dissipation rate, but this is only a small fraction of the *total* dissipation rate, which is now dominated by non-breaking contributions. Hence, for all the wave age conditions observed, microbreakers make an insignificant contribution to the total wave dissipation rate in the wave boundary layer. We tested the sensitivity of the results to the SM15a whitecap analysis methodology by transforming the SM15a breaking data using our breaking crest processing methodology. This resulted in the small-scale breaking waves making an even smaller contribution to the total wave dissipation rate, and so the result is independent of the breaker processing methodology. Comparison with other near-surface total TKE dissipation rate observations also support this conclusion. These contributions to the spectral dissipation rate in ocean wave models are small and need not be explicitly resolved.

1. Introduction

The evolution of the wave height spectrum is generally modelled via the radiative transfer equation (Komen et al., 1994) assuming deep water and a slowly varying current

$$\frac{\partial \Phi}{\partial t} + \nabla.\left((\mathbf{U} + \mathbf{c}_g)\Phi\right) = \mathrm{S}_{wave} = \mathrm{S}_{in} + \mathrm{S}_{nl} + \mathrm{S}_{ds}$$

where $\Phi(\mathrm{k}, \theta)$ is the directional wave spectrum, $\mathbf{c}_g$ is the group velocity and $\mathbf{U}$ is the current. The total source term $S_{wave} = S_{in} + S_{nl} + S_{ds}$, where S_{in} is the atmospheric input spectral source term, S_{nl} is the nonlinear spectral transfer source term representing nonlinear wave-–wave interactions and S_{ds} is the total spectral dissipation rate. S_{ds} is comprised of a breaking wave contribution S_{ds}^{br} and a wave dissipation rate component S_{ds}^{nb} associated with allied turbulent boundary layer processes other than breaking waves. The latter becomes dominant during old wind sea conditions.

An important aspect of these three primary source terms is the spectral bandwidth needed to properly capture the underlying physics. There is extensive literature on the spectral distribution of the wind input and nonlinear spectral interactions, but the relative importance of different wave scales in the wave breaking dissipation rate source term S_{ds}^{br} has remained elusive. The recently-developed measurement capability of imaging and analysing microbreakers reported by Sutherland and Melville (2013) and used in Sutherland and Melville (2015a, hereafter SM15a) has made it possible to investigate their relative importance in the dissipation rate source term (S_{ds}).

1.1. Breaking wave scales

Unlike whitecaps, breaking gravity-capillary and gravity wavelets which do not entrain air have been referred to as microscale breakers (hereafter microbreakers) (e.g. Phillips and Banner, 1974). In fresh water, their wavelengths are reported to range from O(0.05–0.7 m) (Caulliez, 2011). Salinity and surface tension may modify the breaking-induced aeration process, possibly influencing reported microscale breaker wavelengths, e.g. O(0.1–1 m), Jessup and Zappa, 1997; (0.1–0.5 m), Frew et al., 2004; (0.05–0.3 m), Dimas, 2007, among

* Corresponding author.
E-mail addresses: m.banner@unsw.edu.au (M.L. Banner), r.morison@unsw.edu.au (R.P. Morison).

https://doi.org/10.1016/j.ocemod.2018.04.004
Received 26 January 2018; Received in revised form 9 April 2018; Accepted 17 April 2018
Available online 18 April 2018
1463-5003/

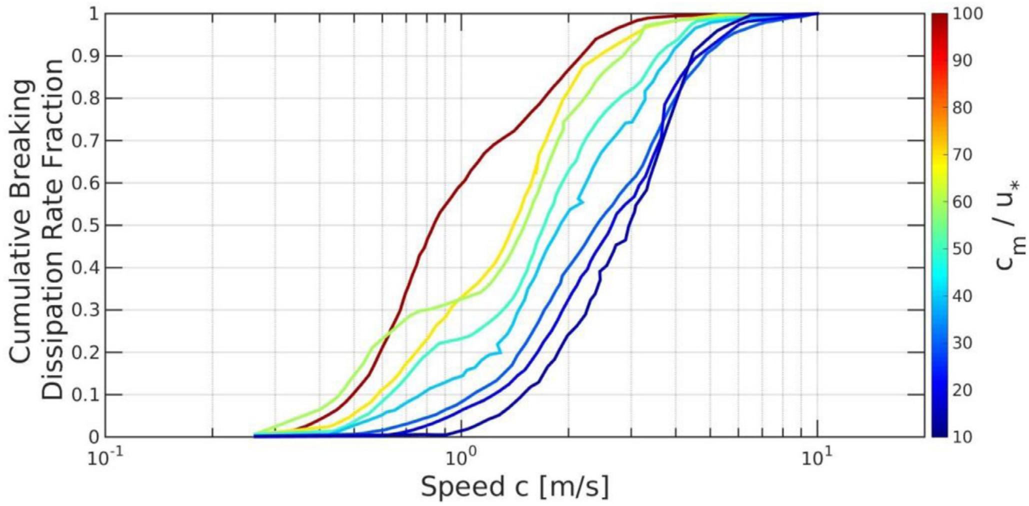

Fig. 1. Cumulative breaking wave dissipation rate () normalised by the total breaking wave dissipation rate (S_{ds}^{br}), as a function of breaking front speed (c) for the range of wave age (c_m/u_*) conditions shown in the colour bar. This figure is derived from Fig. 7 in SM15a. (For interpretation of the references to colour in this figure legend, the reader is referred to the web version of this article.)

others. Reference to histograms showing breaking crest segment count N against breaker speed c_b in the two centre panels in Fig. 2 of Gemmrich et al. (2013), confirms the presence of small whitecaps with speeds below 1 m/s for representative young and old wind sea conditions. Note that the whitecap speeds were assigned according to initial breaker front speed. From that figure, $c < 1$ m/s is seen to be a generous upper limit for the speed of microbreakers, and the highest whitecap counts were found for $1 < c < 2$ m/s, with $0 < c < 1$ m/s (and $2 < c < 3$ m/s) not much smaller, summed over all wave ages. Given the observed co-existence of small whitecaps with microbreakers for $c < 1$ m/s, we define microbreakers as breaking waves with speed $c < 1$ m/s, which are predominantly non air-entraining. Assuming the linear dispersion relation, this corresponds to wavelengths $\lambda < 0.64$ m and intrinsic frequencies $f > 1.55$ Hz. These wavelengths are approximate as the dispersion relation may not be exact for breaking crests (see Appendix A). Small air-entraining breaking waves (hereafter 'small whitecaps') are defined here as those with $1 < c < 2$ m/s, $0.64 < \lambda < 2.56$ m and $0.8 < f < 1.55$ Hz. Note that the $c = 2$ m/s threshold was chosen by SM15a in their Fig. 7 (replotted in Fig. 1) to quantify the dissipation rate of contributions from microbreakers.

The present study aims to review the latest measurements of this poorly understood high wavenumber aspect of the sea surface microstructure and assess its importance for the turbulent dissipation rate (ε_{tot}) in air-sea interfacial physics and modelling. It is well-recognised that turbulent kinetic energy is injected sporadically at the wind-driven sea surface under active wave-breaking conditions (e.g. Craig and Banner, 1994; Melville, 1994; Terray et al., 1996). TKE dissipation rates (ε_{tot}) have been linked to air-sea gas transfer rates (Zappa et al., 2007) and to sea spray production rates (Veron, 2015). The breaker scale bandwidth and spatio-temporal frequencies depend primarily on wind speed and wave age. Young wind seas experience a higher probability of breaking of longer waves, which decreases as the wind seas age. For old seas, the predominant breaking scale transitions towards small whitecaps and microbreakers (Gemmrich et al., 2013). The spectral distribution of breaking wave dissipation rate ($S_{ds}^{br}(c)$) contributions to the total wave dissipation rate (S_{ds}) in the wave boundary layer is not known accurately, as robust *direct* measurements are presently not available.

Understanding the physics and quantifying the total wave dissipation rate ($\int S_{ds}(k)dk$) in the upper ocean, including the wave boundary layer, has attracted considerable interest over recent decades. The turbulent kinetic energy (TKE) dissipation rate profile (ε(z)) decreases rapidly with depth z below the surface, and $\varepsilon_{tot} = \int_{-20}^{\eta} \varepsilon(z)dz$, the depth integration of ε(z) over the wave boundary layer. Since we are unable to directly measure the wave dissipation rates (S_{ds}) and (S_{ds}^{br}), the total TKE dissipation rate (ε_{tot}) is used as the best measured estimate of the total wave dissipation rate (S_{ds}) (Gemmrich, 2010; Zappa et al., 2016; Schwendeman et al., 2014 who all assumed $S_{ds} = S_{ds}^{br}$). There has also been ongoing debate on how well the wave boundary layer is described by turbulent wall-layer scaling, for which the local TKE dissipation rate ε_{wl}(z) at mean depth z below the ocean surface is given by:

$$\varepsilon_{wl}(z) = \frac{u_{*w}^3}{\kappa z}$$

where $\kappa \sim 0.41$ is the von Karman constant, $u_{*w}$is the water-side friction velocity (e.g. Terray et al., 1996). However, recent consensus strongly favours a breaking-wave enhanced layer for a range of conditions, where the near-surface TKE dissipation rate ε(z) exceeds the wall layer estimate ε_{wl}(z) by a considerable margin. Section 1 in SM15a presents a state-of-the-art account of this extensive literature as a lead-in to their paper describing their recent measurements and findings on this challenging topic.

Briefly, new insights are emerging as a result of novel measurement techniques and analyses reported in recent field investigations (SM15a; Wang et al., 2013). These studies have provided comprehensive results for a broad range of open water wind and sea-state conditions that link refined subsurface dissipation rate measurements, novel surface dissipation rate measurements and co-located surface wind and wave properties (e.g. Gemmrich, 2010; Schwendeman et al., 2014; SM15a). This includes spectrally-resolved measurements of whitecap kinematics, from which spectral breaking wave dissipation rates ($S_{ds}^{br}(c)$) can be estimated using Phillips (1985) (hereafter P85) spectral breaking wave framework and its recent refinements (e.g. Banner and Morison, 2010; Romero et al., 2012, hereafter R12). These studies revisit key open questions, including the dependence of the depth-integrated TKE dissipation rate (ε_{tot}) on wind speed and wave age, with a special focus on the contribution made by breaking waves. Throughout this paper, we use the term wave age to denote the mean wave age c_m/u_* parameter adopted in SM15a, where u_* is the wind friction velocity and c_m is a characteristic measure of the wind wave speed. This wave age was considered in Section 2c of SM15a to be more closely related to the breaking wind-waves than the usual spectral peak wave age c_p/u_*, which can be representative of swell. Here, $c_m = g/\omega_m$, where g is gravity and ω_m is the mean frequency computed from the frequency spectrum $S_{\eta\eta}(\omega)$ as:

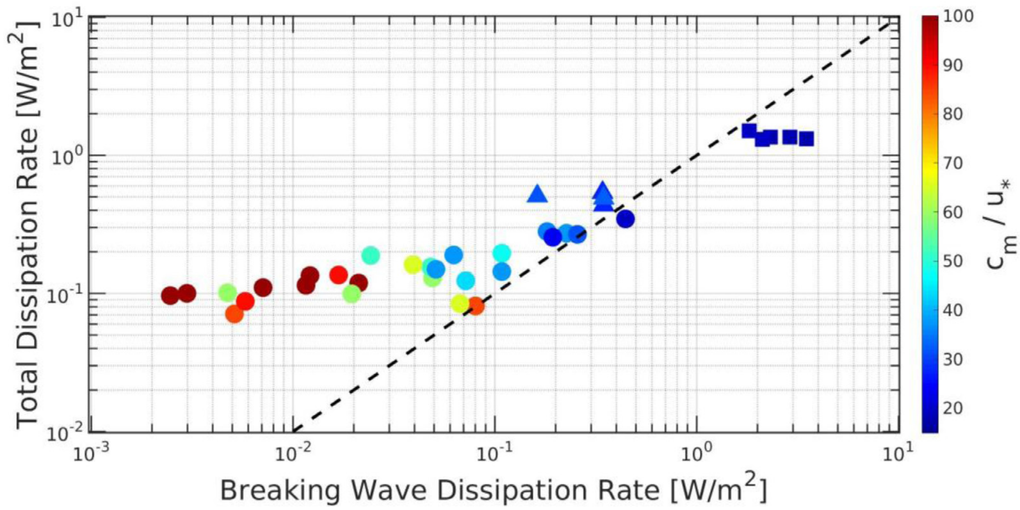

Fig. 2. Measured total TKE dissipation rate (ε_{tot}) integrated across the wave boundary layer to 20 m depth against the breaking wave dissipation rate integrated over all resolved wave scales (S_{ds}^{br}), redrawn from Fig. 16 in SM15a. The range of wave age (c_m/u_*) conditions from developing wind seas to old swell is indicated in the attached colour bar. (For interpretation of the references to colour in this figure legend, the reader is referred to the web version of this article.)

$$\omega_m = \frac{\int_0^\infty \omega s_{\eta\eta}(\omega)d\omega}{\int_0^\infty s_{\eta\eta}(\omega)d\omega}$$

In this context, the relative importance of the different scales of breaking waves from large whitecaps to microbreakers has emerged as a new element. In their recent measurements investigating active whitecap coverage, Schwendeman and Thomson (2015) reported lower correlation with dissipation rate than with wind or wave conditions, with residuals showing a strong negative trend with wave age. They suggested that the discrepancy is likely due to the increased influence of microbreakers in older wind seas (referencing SM15a for justification).

In this paper, we focus on the important issue of the relative contributions of the different breaking wave scales to the total wave dissipation rate (S_{ds}) in the wave boundary layer and how this changes for different wave ages. Based on the recent comprehensive study of SM15a, our study investigates the relative importance of the contribution of microbreakers and small whitecaps. This topic is of central importance as wave breaking is a key air-sea interaction process, whose sea surface expression in the form of whitecapping or microbreaking is currently under active investigation. In global sea state models, it is important to know the shortest resolved wave scale that should be included explicitly or parametrically in order to capture the dominant physics. Currently, NCEP's WaveWatch III operational frequencies range from 0.035 Hz to 0.96 Hz (Chawla et al., 2013). The corresponding speed of 0.96 Hz waves is 1.63 m/s. Also, there are several important scientific processes and applications associated with this phenomenon, including fundamental air-sea interfacial fluxes and the utilisation of breaking wave signatures as a remote sensing tool for inferring these fluxes.

We reanalysed the data of SM15a, supplemented by the near-zero fetch Lake Michigan data of Wang et al. (2013) (hereafter W13). This provided new insights on the subsurface dissipation rates ($\varepsilon(z)$) of microbreakers and small whitecaps in greater isolation. In their more recent data analysis sensitivity study, Wang and Liao (2016) (hereafter W16) revisits the same near-zero fetch data reported in W13. SM15a suggests, and W16 concurs (referencing SM15a to justify), that the high dissipation rate level observed within O(100 mm) of the sea surface is consistent with a large fraction of the wave energy dissipation rate (S_{ds}) being attributed to microbreakers. In this paper, we review the relative contributions of microbreakers and small whitecaps to the breaking (S_{ds}^{br}) and total (S_{ds}) wave dissipation rates in the wave boundary layer.

2. Key results from Sutherland and Melville (2015a)

SM15a combines their novel infrared geometric/kinematic breaking wave crest length spectral density measurements ($\Lambda(c)$) from Sutherland and Melville (2013) with parametric spectral breaking strength coefficients from spectral wind-wave modelling (R12), to infer the dissipation rate ($S_{ds}^{br}(c)$) contribution from breaking wave scales ranging from large whitecaps to microbreakers. These results are described and reported in detail in SM15a. While the breaking front imagery allows extraction of directional distributions of $\Lambda(c,\theta)$, the results presented are for the azimuthally-integrated distribution

$$\Lambda(c) = \int_0^{2\pi} c\Lambda(c,\,\theta)\mathrm{d}\theta$$

The integrated dissipation rate contribution from all resolved breaking wave scales is given by the fifth moment of $\Lambda(c)$, weighted by the spectral breaking strength coefficient b according to:

$$S_{ds}^{br} = \int S_{ds}^{br}(c)dc = \frac{\rho_w}{g}\int bc^5\Lambda(c)dc$$

(P85; Banner and Morison, 2010; R12; SM15a), where ρ_w is the water density and g is the gravitational acceleration.

Figs. 6, 7 and 16 in SM15a provide the basis for our analysis, as they contain the data relevant to assessing the relative importance of the microbreaker and small whitecap contributions to both the breaking wave dissipation rate (S_{ds}^{br}) and total wave dissipation rate (S_{ds}).

The data from Fig. 7 in SM15a are redrawn in Fig. 1 below. This figure shows the cumulative integral of the spectral breaking wave dissipation rate ($S_{ds}^{br}(c)$) normalised by the total breaking wave dissipation rate (S_{ds}^{br}) for each measured wave age case. It should be noted that this figure only addresses contributions relative to the breaking wave dissipation rate (S_{ds}^{br}), not to the total wave dissipation rate (S_{ds}).

A second key figure underpinning our analysis is Fig. 16 in SM15a, redrawn as Fig. 2. This shows the measured TKE dissipation rate integrated over the top 20 m of the ocean (ε_{tot}), plotted against the breaking wave dissipation rate (S_{ds}^{br}) integrated over all resolved wave scales, for a range of wave ages from developing wind seas to old swell. As seen on the left side of Fig. 2, where the total TKE dissipation rate (ε_{tot}) is much larger than the breaking wave dissipation rate (S_{ds}^{br}) for old seas, there is a contribution to the TKE dissipation rate (ε_{tot}) in the wave boundary layer not directly related to breaking but from other hydrodynamical processes. These include the influence of surface waves on the Reynolds shear and normal stresses from the subsurface turbulence, and resulting energy transfer between the waves and the turbulence.

This is important in quantifying the wave energy dissipation rate (S_{ds}^{nb}) due to the interaction between non-breaking waves and turbulence, which is a source of wave damping additional to wave breaking. Other non-breaking sources of turbulence are discussed in SM15a, Section 6b.

The recent paper by Guo and Shen (2014) includes a comprehensive literature review of this topic. In the more complex oceanic context, Sullivan and McWilliams (2010) highlighted the need to include Langmuir turbulence, larger wavenumber bandwidth and directional spreading of the surface waves in the non-breaking dissipation rate (S_{ds}^{nb}) contributions. In the present paper, the background wave dissipation rate (S_{ds}^{nb}) is taken as that arising from all sources other than turbulence actively injected by breaking waves.

The key challenges investigated in this paper are to quantify, as the seas evolve: (i) the fractional contribution of breaking waves to the total wave dissipation rate (S_{ds}); (ii) the relative importance of microbreakers and of small whitecaps to the breaking (S_{ds}^{br}) and total (S_{ds}) wave dissipation rates.

3. Reanalysis of the data in Section 2 of Sutherland and Melville (2015a)

Fig. 3 indicates that for the high TKE dissipation rates (ε_{tot}) in developing wind seas (right side of plot), wave breaking accounts for almost all of the total TKE dissipation rate (ε_{tot}). However, for old wind seas (left side of plot), wave breaking contributes only a small fraction of the total TKE dissipation rate (ε_{tot}). Using this data, the fraction of the dissipation rate contributed by wave breaking (S_{ds}^{br}) to the total dissipation rate (ε_{tot}) is plotted against the wave age in Fig. 4.

In Fig. 4, it is seen that for the younger wind seas, the mean breaking dissipation rates inferred from measurements/modelling account for the total measured TKE dissipation rate (ε_{tot}), within the error bars reported in SM15a. However, as the seas age, this fraction decreases until it becomes insignificant ($<5\%$). The black dashed line in Fig. 4 is a linear least-squares fit to the SM15a data. This data (and the fitted black dashed curve) extend above the physically allowable maximum value of 1, likely due to measurement/modelling uncertainties. For our subsequent analysis we replaced the dashed black curve by the solid red line fit which asymptotes to just below 1.

A key aspect of Fig. 1 (Fig. 7 in SM15a) is that it does not show the absolute levels for the breaking dissipation rate (S_{ds}^{br}), for each of the wave age cases. However, this information is essential to assess the relative importance of different wave breaking scales to the total wave dissipation rate (S_{ds}) in the wave boundary layer. We were able to extract this information from the b-weighted fifth moment spectra of $\Lambda(c)$ provided in Fig. 6(d) of SM15a, which we integrated. This figure is redrawn as Fig. 5 and was used to plot the cumulative breaking wave dissipation rate ($S_{ds}^{br}(c)$) as a fraction of the total wave breaking dissipation rate (ε_{tot}) in Fig. 6.

In Fig. 6(d) of SM15a, the breaking wave dissipation rate is defined as: $S_{ds}^{br}(c) = b\ c^5\Lambda(c)$ ($\mathrm{m^3\ s^{-4}}$). In this figure, the breaking crest length spectral density, $\Lambda(c)$, was measured in three different field experiments. The breaking strength coefficient b is a function of the spectral saturation B, unlike in P85 where b was assumed constant. We used the same breaking strength formulation as SM15a so that any difference in conclusions does not depend on the choice of b. Here $b = b(\mathrm{B})$ is calculated following the spectral saturation-based breaking strength parameterisation developed by R12, described by Eq. (5) in SM15a. In Fig. 5, the line colours and corresponding average wave age bins are the same as used in Fig. 1. While this data is quite noisy due to the variability of $b(\mathrm{B})$, it is readily integrated to obtain a reasonable estimate of the mean total dissipation rate for each of the average wave age bins in Fig. 1.

Using the data in Fig. 6a together with the average c_m/u_* for each bin and the red curve fit in Fig. 4, the corresponding average total wave dissipation rate (S_{ds}) was calculated for each of the average wave age bins plotted in Fig. 5. The breaking wave dissipation rate was plotted as a fraction of the total wave dissipation rate against breaker speed c, for the wave age bins in Figs. 1 and 5, and is shown in Fig. 6b.

Fig. 6 highlights the following key points:

(i) For young seas, the integrated breaking dissipation rate (S_{ds}^{br}) is a large percentage of the total dissipation rate (S_{ds}), whereas for old seas, it is only a small fraction of the total dissipation rate (S_{ds}).
(ii) For young seas, the larger-scale breaking waves make a substantial relative contribution to the total wave dissipation rate, whereas for old seas, only the small breaking waves contribute to the total dissipation rate. Hence, for old wind seas, the larger-scale breaking waves make a negligible contribution to the wave dissipation rate. This can also be seen in Fig. 5.
(iii) For old seas, breaking waves only make a small ($<10\%$) contribution to the total wave dissipation rate, with microbreakers only making a very small contribution. Also, for young seas, microbreakers ($c < 1$ m/s) contribute $<8\%$ and microbreakers together with small whitecaps ($c < 2$ m/s) make up $<26\%$ of the

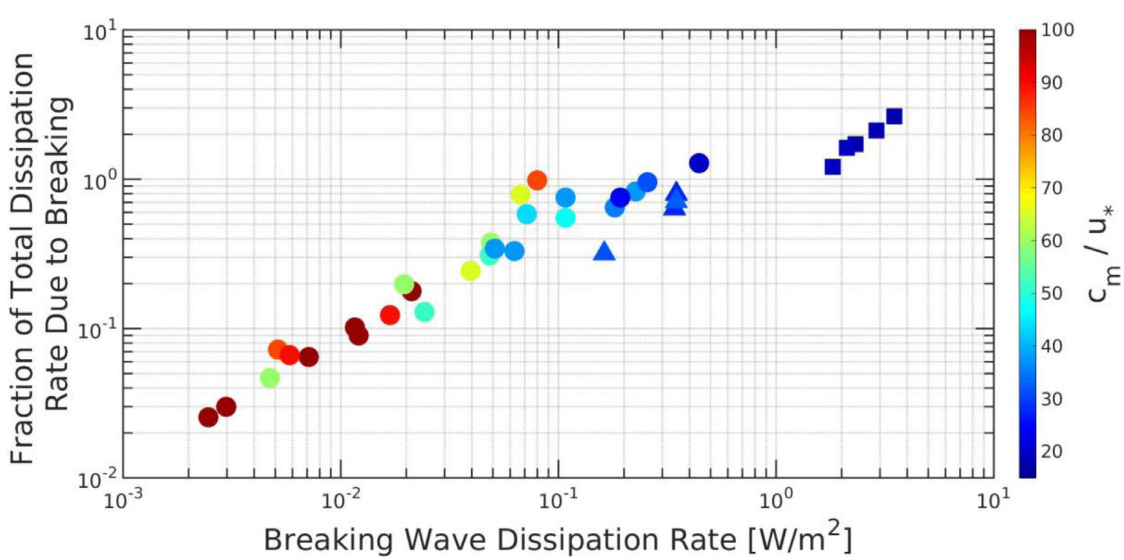

Fig. 3. Replot of the data in Fig. 2, retaining the horizontal axis, symbols and colours. The vertical axis now shows the fractional contribution of the breaking wave dissipation rate (S_{ds}^{br}), to the total measured dissipation rate (ε_{tot}) in the wave boundary layer. (For interpretation of the references to colour in this figure legend, the reader is referred to the web version of this article.)

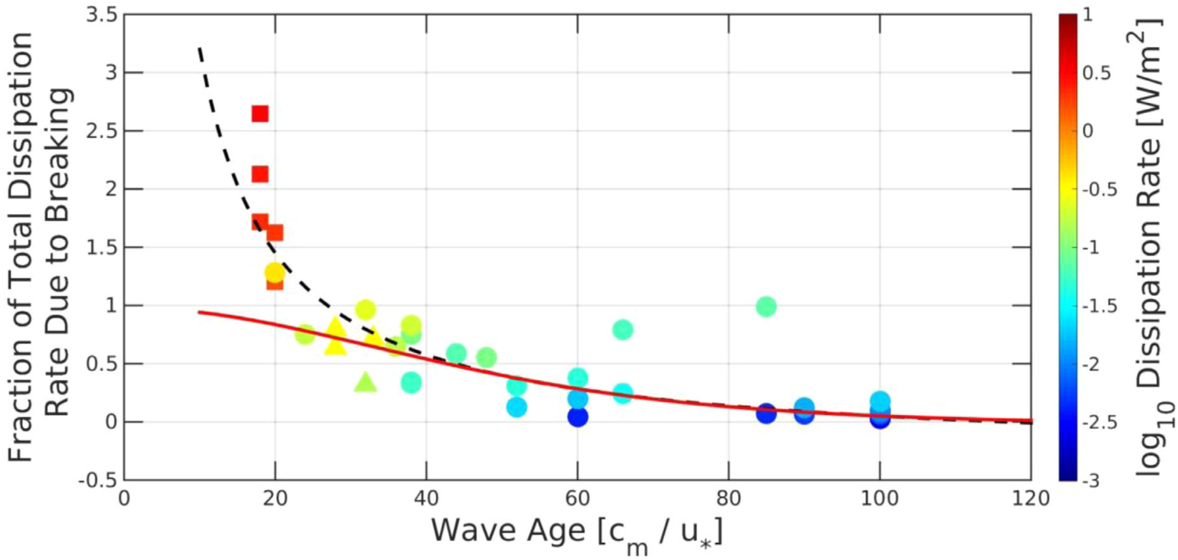

Fig. 4. Fraction of the total dissipation rate due to breaking $(S_{ds}^{br})/(S_{ds})$, plotted against wave age c_m/u_*. The colours represent $\log_{10}$ of the total TKE dissipation rate (ε_{tot}). This figure is a transformation of the data in Fig. 3. The solid red and black dashed curves are two fits to the data, as explained in the text. (For interpretation of the references to colour in this figure legend, the reader is referred to the web version of this article.)

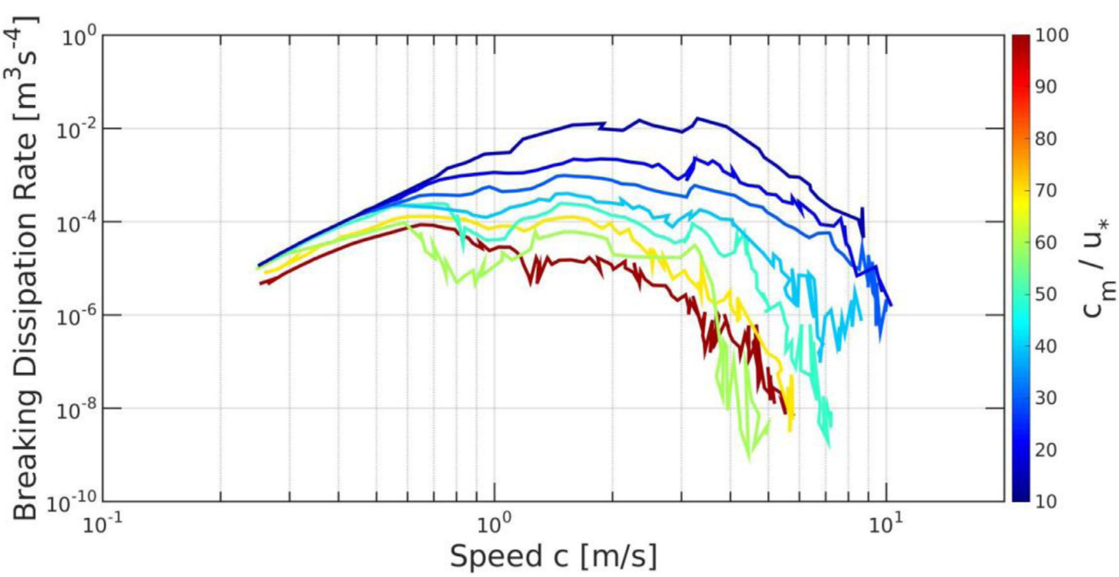

Fig. 5. Spectral breaking dissipation rate () versus speed c (from Fig. 6(d) in SM15a). (For interpretation of the references to colour in the text, the reader is referred to the web version of this article.)

total wave dissipation rate.

To elucidate further the relative contribution to the total wave dissipation rate made by all breaking wave fronts with speeds below a particular speed, the low wave speed results in Fig. 6 were extracted and replotted in Fig. 7.

Fig. 7 is a centrepiece figure for this paper, and encapsulates some of the major findings which are based on the methodology of SM15a:

(i) Microbreakers travelling at speeds less than 0.5 and 1.0 m/s never contribute more than 3% and 8% of the total wave dissipation rate (S_{ds}) respectively.
(ii) Small whitecaps, plus microbreakers, travelling at speeds less than 1.5 and 2 m/s never contribute more than about 16% and 26%, respectively to the total wave dissipation rate (S_{ds}).
(iii) These contributions reduce to less than 5% for old seas, where active breaking only plays a small role in the total wave dissipation rate (S_{ds}).

4. Sensitivity to breaking wave image processing methodology

This section highlights the results of our alternative $\Lambda(c)$ extraction methodology, described in detail in Appendix A. We review in detail the sensitivity of the main findings in Section 3 of SM15a to the measured $\Lambda(c)$ processing methodology.

In brief, during active breaking, a breaker crest front slows down to about half its initial velocity (Kleiss and Melville, 2011, Fig. 13c; Gemmrich et al., 2013, Fig. 1). This intrinsic unsteadiness results in a significant difference in the $\Lambda(c)$ distributions from each method, because each method assigns a different velocity to a given detected breaking front. In Appendix A, we describe in detail how our methodology assigns the initial speed of each breaker (corrected to the intrinsic speed of the underlying wave) in determining the $\Lambda(c)$ contribution for that breaking event. However, SM15a assigns the

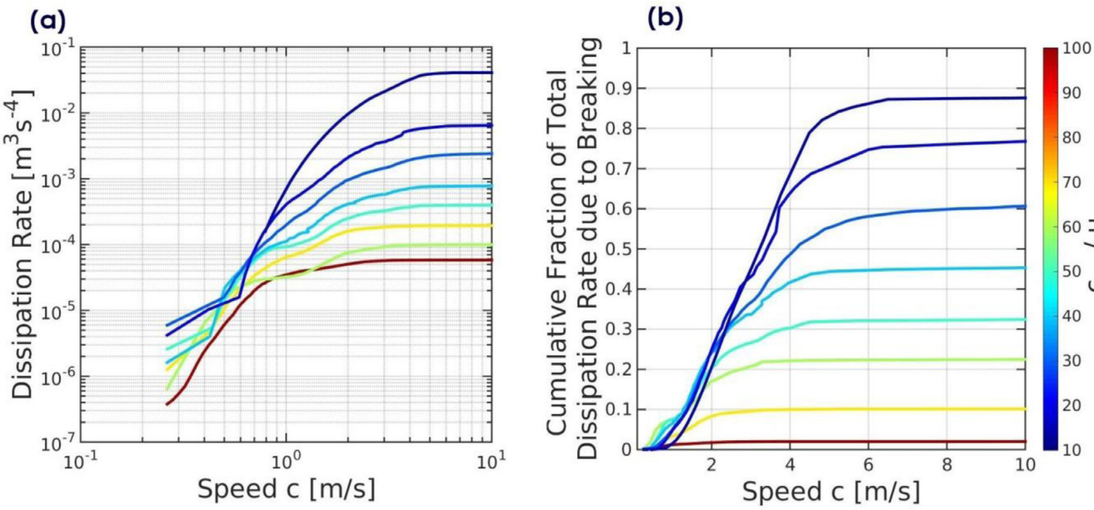

Fig. 6. (a) cumulative breaking wave dissipation rate of against breaker speed for a range of average wave age bins, for the experiments reported in SM15a. (b) cumulative breaking wave dissipation rate of as a fraction of total wave dissipation rate (S_{ds}) plotted against breaker speed c. The colours represent average wave age (c_m/u_*) bins for both panels, and are the same as in Figs. 1 and 5. (For interpretation of the references to colour in this figure legend, the reader is referred to the web version of this article.)

instantaneous speed determined at each video time-step of each individual slowing breaking crest front length, and builds the $\Lambda(c)$ distribution from these different speed bins. This method progressively assigns the later stages of each evolving breaking crest front length to slower speed bins (as the breaker slows down). Overall, this biases their derived $\Lambda(c)$ distribution to lower wave speeds. Repeating the calculations in Section 3 above using our corrected, alternatively processed $\Lambda(c)$ distribution leads to the results in Fig. 8.

Clearly, Fig. 8 not only parallels the results shown in Fig. 7 and conclusions based on the $\Lambda(c)$ methodology of SM15a, but further diminishes the role of the microbreakers. Using our transformed $\Lambda(c)$:

(i) Microbreakers travelling at speeds less than 0.5 and 1.0 m/s never contribute more than 1% and 3% of the total wave dissipation rate (S_{ds}), respectively.
(ii) Small whitecaps, combined with microbreakers, travelling at speeds less than 1.5 and 2 m/s never contribute more than about 6% and 15%, respectively.
(iii) These contributions reduce to less than 2% for old seas, where active breaking only plays a small role in the total wave dissipation rate (S_{ds}).

Thus comparing the results in Figs. 7 and 8 indicates that both methodologies lead to the same conclusion that microscale breakers never contribute significantly to the total wave dissipation rate (S_{ds}) for any wave age, with our $\Lambda(c)$ methodology strongly supporting these conclusions.

5. Comparison with near-surface total dissipation rate observations

It is of fundamental interest to relate these IR imagery-based and

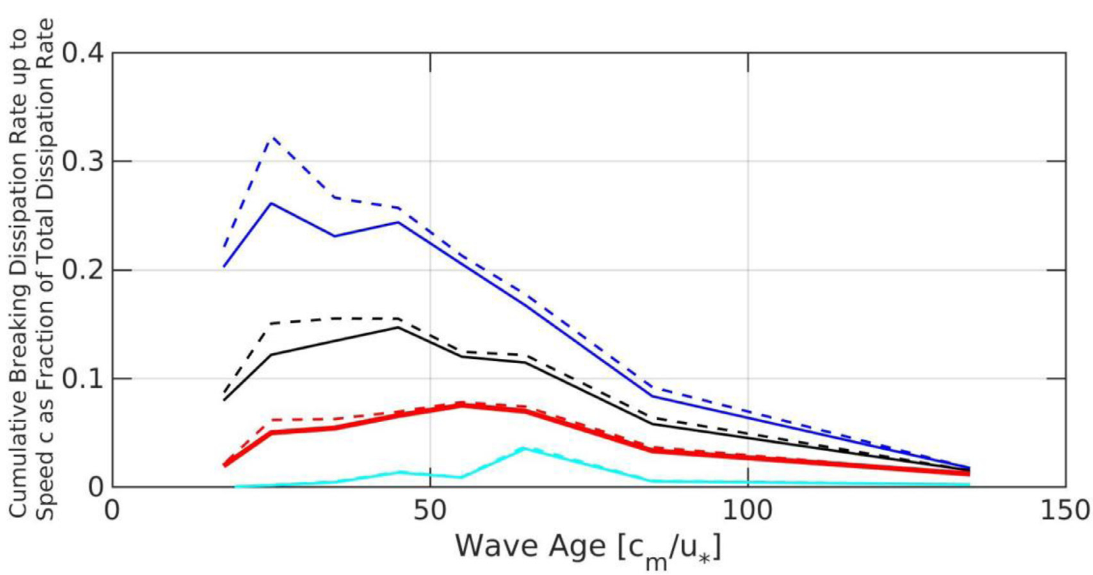

Fig. 7. Cumulative breaking dissipation rate of from breaking fronts with speeds up to c (m/s) as a fraction of the total wave dissipation rate (S_{ds}), plotted against wave age, for c = 0.5 m/s (cyan), c = 1 m/s (red), c = 1.5 m/s (black) and c = 2 m/s (blue). The solid and dashed lines are based, respectively, on the solid red line and black dashed line fits to the data in Fig. 4. (For interpretation of the references to colour in this figure legend, the reader is referred to the web version of this article.)

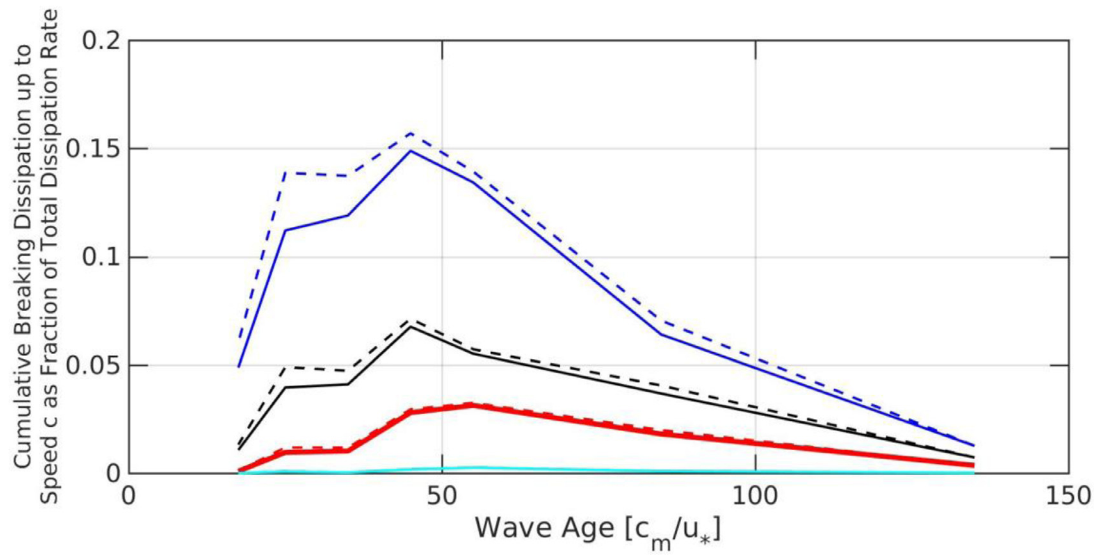

Fig. 8. Same as Fig. 7, but using our transformed estimates for $\Lambda(c)$ as described in Appendix A. Note the vertical scale is half that used in Fig. 7. Cumulative breaking dissipation rate of from breaking fronts with speeds up to c (m/s) as a fraction of the total wave dissipation rate (S_{ds}), plotted against wave age, for $c = 0.5$ m/s (cyan), $c = 1$ m/s (red), $c = 1.5$ m/s (black) and $c = 2$ m/s (blue). The solid and dashed lines are based, respectively, on the solid red line and black dashed line fits to the data in Fig. 4. (For interpretation of the references to colour in this figure legend, the reader is referred to the web version of this article.)

visible breaking wave dissipation rate (S_{ds}^{br}) estimates with the measured total TKE dissipation rate (ε_{tot}), from vertical profiles in the open ocean wave boundary layer. SM15a provides a comprehensive data set of the latter, comprising both fixed and floating Aquadopp deployments, for a range of wind and sea state conditions ranging from developing to very mature seas. To complement their subsurface measurements, a novel surface vorticity approach using IR PIV measurements, Sutherland and Melville (2015b, hereafter SM15b), was used to quantify the total TKE dissipation rate (ε_{tot}) at the air-sea interface. The SM15a subsurface measurements approached within O (70 mm) of the sea surface, leaving a shallow but energetically-significant, near-surface layer with no measurements. In this unresolved layer, a strong increase in the TKE dissipation rate (ε(z)), towards the surface is required to match to the SM15a IR-measured surface levels. Does the dissipation rate from microbreakers and/or small whitecaps explain this high near-surface dissipation rate?

We investigate this further by collating results from two studies where the TKE dissipation rate (ε_{tot}) from microbreakers and small whitecaps was measured in ‘isolation’ from the longer waves and background subsurface dissipation rate (ε(z)) present in open ocean studies. As such, they are able to capture the order of magnitude of the contributions to the total wave dissipation rate (S_{ds}) from the very short breakers when they are at the spectral peak, for wind speeds corresponding to the open ocean TKE dissipation rate (ε_{tot}) data, as shown below.

Fig. 9 shows the SM15a open ocean TKE dissipation rate (ε(z)) profiles with depth for the wide range of wind speed (and wave age) conditions observed. Also shown superposed in Fig. 9 are two additional data sets of W13 and Siddiqui and Loewen (2007) (hereafter SL07) that provide significant insight on the indicative strength of the microbreaker and small whitecap contributions to the subsurface TKE dissipation rate (ε(z)) profile with depth. When suitably integrated over depth, their relative contribution to the total TKE dissipation rate (ε_{tot}) in the wave boundary layer can then be estimated.

The detailed study of SL07 is included as it used simultaneous DPIV (digital particle image velocimetry) and infrared imagery to investigate the TKE dissipation rate (ε(z)) profile in near-surface flows immediately below laboratory wind waves at a fetch of 5.5 m and wind speeds from 4.5 to 11 m/s (U_{10} = 6.3 to 18.6 m/s). These conditions produced short steep microbreakers with wavelengths from 60 mm to 180 mm. The depth-integrated TKE dissipation rate (ε_{tot}) was found to be significantly greater than would occur in a comparable rough wall layer flow.

The closest field counterparts to the SL07 laboratory study are by W13 and W16 which adapted the SL07 DPIV technique for use in open waters. Profiles of TKE dissipation rate (ε(z)) were measured in a field experiment in Lake Michigan under a near-zero fetch condition for different wind speeds, and a short open water fetch condition for a single low wind speed condition. They were able to measure the structure of turbulence in the wave boundary layer to obtain TKE dissipation rate (ε(z)) data up to the instantaneous water surface, using a free-floating underwater miniature DPIV system. Their surface-following configuration allowed measurements of the aqueous-side turbulence statistics in the topmost layer immediately below the water surface down to a local depth of 150 mm. Different data analysis methods to estimate the TKE dissipation rate (ε(z)) were compared, which yielded consistent TKE dissipation rate (ε(z)) profiles within reasonable scatter bounds. TKE dissipation rate (ε(z)) profiles were measured for a variety of wind and wave conditions. W16 suggested that the strong surface skin layer dissipation rate may be attributed to microbreaking (referencing "SM15a suggested that 20–90% of the surface dissipation could be attributed to the non-air entraining breakers") and its downward transport in the water column.

For reference, Table 1. summarises the key properties of the Lake Michigan and laboratory data sets discussed here.

Fig. 9 shows the large contrast between the SM15a open ocean profile data in comparison with the W13 Lake Michigan data and the SL07 laboratory data at the same depth for similar wind speeds. For illustration, for the U_{10} = 12 m/s data at a common depth of 0.1 m, the open ocean TKE dissipation rate (ε(z)) level is O(30) times stronger than both the Lake Michigan near-zero fetch data and the laboratory data. This trend is observed for all the wind speeds shown.

The collation of the available subsurface TKE dissipation rate (ε(z)) profile results from these lake, laboratory and open ocean data sets shown in Fig. 9 can be displayed for specific wind speed bands. This more clearly highlights the relative importance of microbreaker and small whitecap contributions to the observed TKE dissipation rate (ε(z)) profile in the open ocean wave boundary layer. The figures provide a valuable complementary basis for verifying results and conclusions based on the breaking wave analysis.

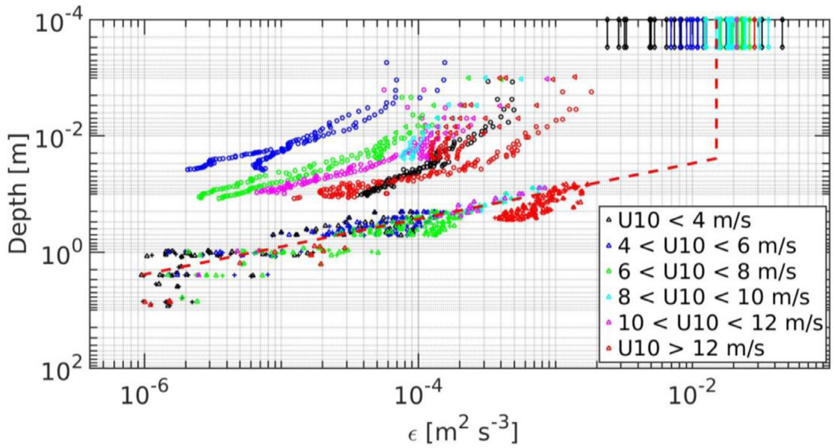

Fig. 9. Local TKE dissipation rate ε(z) (horizontal axis) as a function of depth (z) (vertical axis) for three different experiments. The colours showing wind speed U_{10} are given in the legend. The open circles are Lake Michigan measurements of W13 and left facing triangles are wave tank measurements of SL07; all the other data is from SM15a. Note that the SM15a data is from greater depths and has substantially higher TKE dissipation rates ε(z) than the lake and laboratory studies at matching depths for comparable wind speeds. The data at depths (1–3) × 10^{-4} m at the top right show the surface TKE dissipation rate data from SM15a. (For interpretation of the references to colour in this figure legend, the reader is referred to the web version of this article.)

Table 1
Summary of wind and wave conditions during the SL07 laboratory and W13 field studies. U_{10} and u_{*a} are the 10 m wind speed and wind friction velocities; ω_p is the spectral peak frequency, λ_p is the dominant wavelength, H_s is the significant wave height and $H_s k_p/2$ is the significant steepness of the wind waves.

SL07 laboratory measurements						
U_{10} (m/s)	u_{*a} (m/s)	f_p (hz)	λ_p (m)	H_s (m)	$H_s k_p/2$	c_p/u_{*a}
6.3	0.32	5.2	0.058	0.0043	0.23	0.94
9.1	0.34	4.1	0.093	0.0082	0.28	1.12
11.5	0.46	3.7	0.114	0.011	0.30	0.88
13.5	0.48	3.5	0.128	0.0125	0.31	0.93
18.6	0.63	3.0	0.176	0.0176	0.31	0.83
W13 Lake Michigan measurements						
U_{10} (m/s)	u_{*a} (m/s)	ω_p (rad/s)	λ_p (m)	H_s (m)	$H_s k_p/2$	c_p/u_{*a}
4.9	0.20	8.64	0.825	0.0218	0.063	5.7
10.0	0.42	5.89	1.77	0.0475	0.084	4.6
7.6	0.30	10.61	0.55	0.0229	0.131	3.6
14.3	0.66	6.28	1.56	0.087	0.175	2.7
2.7	0.12	1.85	18.0	0.35	0.061	45.9

These figures highlight key differences between typical TKE dissipation rate (ε(z)) profiles in laboratory and extremely short fetch open water conditions, for corresponding wind speeds. For each of the wind speed bands shown, the indicative contributions of the near zero-fetch data are both lower in strength and shallower in depth by 1.5–2 orders of magnitude. However, the low wind speed band (< 4 m/s) is only about 1 order of magnitude lower.

Integrated values for these TKE dissipation rate (ε(z)) profile data in the upper 100 mm of the surface layer for the microscale breaker and small whitecap dissipation rate contributions are shown in Fig. 11a. To be able to make meaningful comparisons with the SM15a results, the data was extrapolated to 20 m depth following the SM15a Section 6a methodology, which assumed a depth dependence of z^{-2}. The cumulative depth integrals of these extrapolations are shown in Fig. 11b. These profiles are used to estimate the total TKE dissipation rate (ε_{tot}) from each of the Lake Michigan field data sets for different wind speed cases.

These total TKE dissipation rate (ε_{tot}) levels were then compared with the *breaking wave* dissipation rate (S_{ds}^{br}) estimates for different short breaking wave bandwidths, based on the results described in Section 3 above. Fig. 12 shows the relationship between wind speed and wave age **for the SM15a data**. The black line shows a fitted curve which was used to transform the cumulative results in Fig. 6a to be a function of wind speed, rather than wave age. Since the W13 data were collected at near-zero fetch, there are no larger waves, and the breaking waves are only microbreakers /small whitecaps. Hence, it is impractical to plot the data against wave age.

Using the black curve in Fig. 12, we transformed the SM15a data in Fig. 6a, together with the breaker (S_{ds}^{br}), and measured TKE dissipation rate(ε_{tot}) data from Fig. 3, to show their wind speed dependence. This is plotted in Fig. 13 which encapsulates the main results of this study on the relative importance of microbreakers and small whitecaps to the upper ocean dissipation rate (ε_{tot}).

For the range of wind speed conditions observed in SM15a, Fig. 13 compares the relative levels of the total dissipation rate in: (i) the uppermost 20 m of the ocean; (ii) from microscale and small whitecaps at near-zero fetch, extrapolated to 20 m depth; (iii) from all resolved breaking wave scales; (iv) from microbreakers ($c < 1$ m/s); and (v) from microbreakers and small whitecaps ($c < 2$ m/s).

Fig. 13 shows that the overall ordering of these contributions is both plausible and self-consistent. It is seen that the integrated dissipation rate from all breaking waves (S_{ds}^{br}) (cyan line) matches the total dissipation rate (ε_{tot}) (red line) for the youngest sea conditions where the wind speeds were higher. This progressively reduces towards the lower wind speed, older sea states where the background turbulence level from other sources increasingly dominates. Over the whole range of observations, the microbreaker dissipation rate fractional contribution (blue line) is seen to be O(1%) while the combined fractional contribution of microbreakers and small whitecaps with $c < 2$ m/s, is typically < 5%. With our alternative processing methodology (see Fig. 8), these contributions are halved. The comparable breaking wave dissipation rates reported in SM15a are shown for microbreakers ($c < 1$ m/s) and for microbreakers and small whitecaps ($c < 2$ m/s). The elevated data point at U = 3 m/s is a single measurement in the lake at a short but finite fetch (1.2 km) where the background dissipation rate (S_{ds}^{nb}) exceeded the breaking wave contribution (S_{ds}^{br}).

6. Sources of uncertainty

Several sources of uncertainty underpin the results in the complex suite of measurements and analyses utilised by SM15a. These are discussed in SM15a or in various allied papers by these authors and their collaborators. For example, Fig. 16 in SM15a documents the uncertainty in their integrated dissipation rate (ε_{tot}) measurements, which can be up to one order of magnitude. Fig. 10 in SM15b provides relative uncertainty estimates associated with the estimation of the surface dissipation rate (ε(z)). Kleiss and Melville (2011) discuss various uncertainties associated with extracting crest length spectral density distributions from sea surface visible imagery, with SM13 providing a counterpart for infrared imagery. This aspect includes the contentious issue of breaking front speed assignment, for which uncertainty aspects are investigated in detail in Appendix A. In estimating spectral breaking wave dissipation rates ($S_{ds}^{br}(c)$), a spectral breaking strength formulation

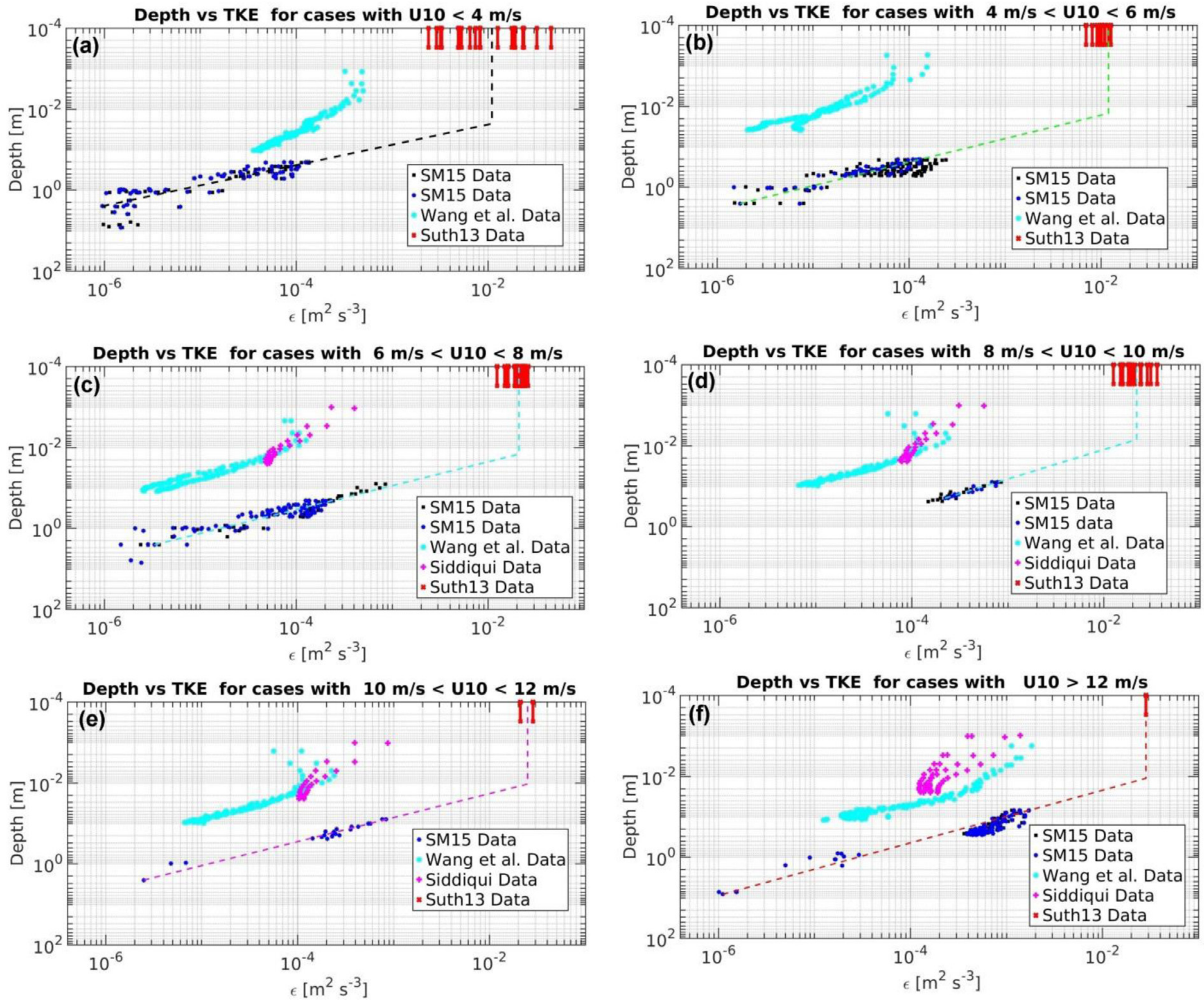

Fig. 10. TKE dissipation rate $\varepsilon(z)$ profiles for the specified wind speed bands from the available laboratory and open water data described in the text. Note: the dataset shown at (1–3) $\times$ 10^{-4} m depth (red) at the top right of each panel shows the IR-based surface dissipation rate data from SM15a. (For interpretation of the references to colour in this figure legend, the reader is referred to the web version of this article.)

is needed. This quantity has a significant uncertainty, as is evident from the paper by R12. We avoided this uncertainty by using the same spectral breaking strength data used by SM15a, which was based on R12. However, this quantity remains a source of significant uncertainty with a potentially large impact on breaking dissipation rate (S_{ds}^{br}) estimates, as pointed out in the discussion of Fig. 4 above. Note that these estimates ignore the contribution of parasitic capillary waves to the overall dissipation rate, which none of the discussed methods are able to resolve. There is also some uncertainty in the non-wave related dissipation contribution to the total TKE dissipation rate (ε_{tot}) as discussed in Section 6b of SM15a.

7. Conclusions

Spectral representations of wave breaking physics are fundamental to modelling the evolution of natural wind wave spectra and air-sea

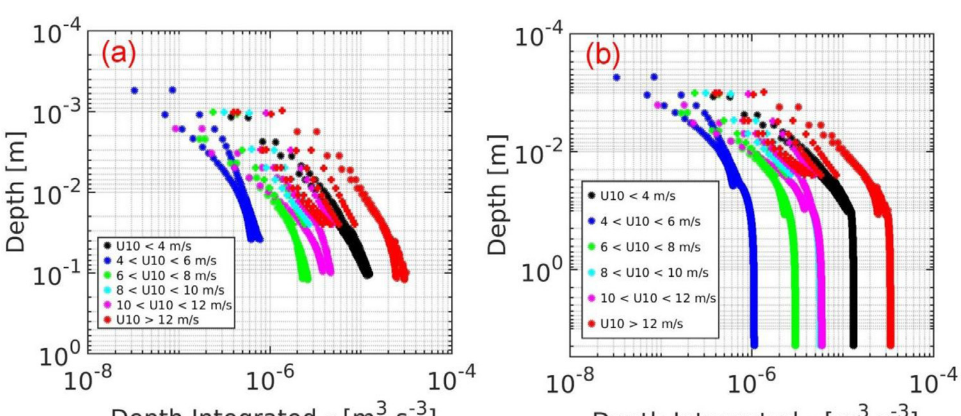

Fig. 11. Cumulative depth-integrated total TKE dissipation rate (ε_{tot}) against depth for the Lake Michigan near-zero fetch and short fetch data of Wang et al. (2013) and Wang and Liao (2016). (a) measured (b) extrapolated to 20 m depth. The very weak falloff of these cumulative integrals with depth seen in (b) is due to the strong z^{-2} falloff assumed in the extrapolated dissipation rate profiles.

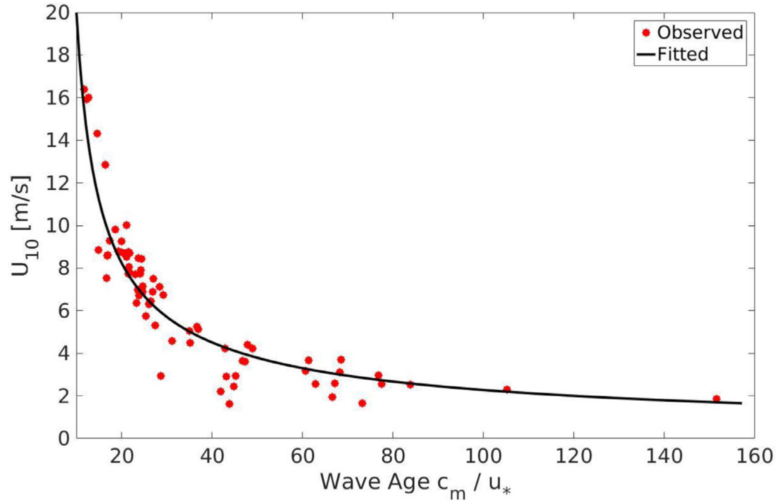

Fig. 12. Relationship between wind speed U_{10} and wave age c_m/u_* for the SM15a data.

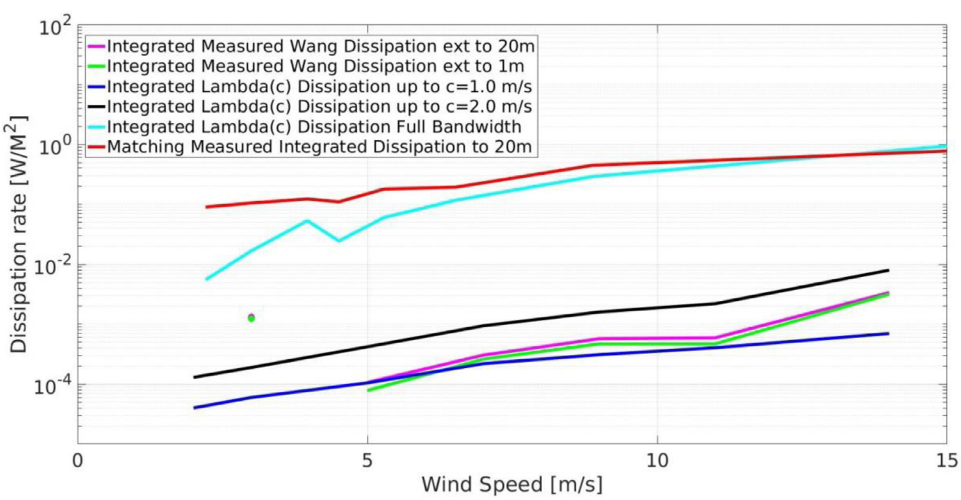

Fig. 13. Comparison of dissipation rate levels from different sources: the red line is the SM15a measured TKE dissipation rate extrapolated to 20 m depth; the cyan line is the SM15a breaker dissipation rate as determined by the full bandwidth integration of $b\rho c^5\Lambda(c)$; the black line is the same as the cyan line, but integrated for $0 < c < 2$ m/s; the blue line is the same as the black line, but integrated for $0 < c < 1$ m/s; the green line is the depth-integrated microbreaker and small whitecap combined dissipation rate measured by W13, extrapolated and integrated to a depth of 1 m, and the magenta line is the same as the green line, but extrapolated and depth-integrated to 20 m. The extrapolations follow SM15a which assumed a z^{-2} depth profile for the dissipation rate. (For interpretation of the references to colour in this figure legend, the reader is referred to the web version of this article.)

interfacial fluxes. It is important to determine what frequencies need to be resolved in models to capture the necessary source term energy fluxes.

To this end, we revisited the findings of recent field studies on surface and near-surface TKE dissipation rates ($\varepsilon(z)$) in the presence of breaking waves. These novel studies embrace surface measurements of the contributions from microbreakers and small whitecaps, and their relation to the subsurface TKE measurements ($\varepsilon(z)$) using acoustic doppler and DPIV techniques immediately below the sea surface.

We reviewed the data analysis methodology used by SM15a which we used to assess the contribution of microbreakers (wave speeds up to 1 m/s) and small whitecaps (wave speeds from 1–2 m/s) to the total wave dissipation rate (S_{ds}). Based on our analysis and the subsurface DPIV studies by W13, we conclude that the contributions of microbreakers and small whitecaps to the total wave dissipation rate (S_{ds}) during active wind-wave generation conditions is far weaker than suggested by SM15a, and is only ever of marginal importance. More specifically:

- For young/developing wind seas, the contributions of microbreakers to the total wave dissipation rate (S_{ds}) is small compared with the contribution from larger-scale breakers.
- For young/developing wind seas, the contributions of small whitecaps to the total wave dissipation rate (S_{ds}) depends on the breaking crest length processing methodology. Using SM15a methodology, small whitecaps contribute up to 20% of the total dissipation rate (S_{ds}), while with our methodology, this reduces to a maximum of 12%.
- For low wind speeds/old seas, microbreakers and small whitecaps dominate the breaking wave dissipation rate (S_{ds}^{br}) contribution. However, the non-breaking dissipation rate (S_{ds}^{nb}) is an order of magnitude larger than the breaking dissipation rate (S_{ds}^{br}).
- For high wind speeds/young seas, microbreakers and small whitecaps make a much smaller contribution to the breaking wave dissipation rate (S_{ds}^{br}).
- Uncertainty in the small breaking wave contributions ($c < 2$ m/s) to the total wave dissipation rate (S_{ds}) results from differences in breaker image processing techniques and uncertainty in the spectral breaking strength coefficient.
- Noting that the corresponding frequency for $c = 1$ m/s is 1.6 Hz, and for $c = 2$ m/s is 0.78 Hz, we estimate that the computational bandwidth used operationally in Wavewatch III which spans from 0.035 to 0.96 Hz will capture at least 95% of the breaking wave dissipation rate.
- The source of the observed elevated dissipation rate levels ($\varepsilon(z)$) in the uppermost 100 mm of the wave boundary layer remains to be determined.

Overall, in regard to the breaking wave dissipation rate (S_{ds}^{br}) and total wave dissipation rate (S_{ds}) in the wave boundary layer, the contributions from microbreakers are negligible and from small whitecaps are secondary. While they may well be important for other processes, these wavenumber scales do not need to be resolved in spectral wave forecast models for quantifying the dissipation rate.

Acknowledgements

The authors gratefully acknowledge the support for our air-sea interaction research from the US Office of Naval Research (Grant N00014-10-1-0390) and the Australian Research Council (DP120101701). We also acknowledge the useful comments from some of the reviewers, whose suggestions have helped us make this paper much clearer.

Appendix A. Impact of alternative $\Lambda(c)$ extraction methodology

This appendix reviews the sensitivity of the main findings in Section 3 of SM15a to the measured $\Lambda(c)$ processing methodology.

A.1. Breaking wave scale

Three methods for analysing breaking wave video imagery are currently used to extract $\Lambda(c)$ from video of breaking waves at sea, with the most appropriate method still to be decided. During active breaking, a breaker crest front slows down to about half its initial velocity (Kleiss and Melville, 2011, Fig. 13c; Gemmrich et al., 2013, Fig. 1). This intrinsic unsteadiness results in a significant difference in the $\Lambda(c)$ distributions from each method, because each method assigns a different velocity to a given detected breaking front. We emphasize that the primary purpose of the $\Lambda(c)$ distribution in P85 was to provide the basis for an accurate, unbiased estimate of the wave energy dissipation rate from breaking, according to wave scale.

The P85 spectral breaking wave framework uses breaking front velocity $\boldsymbol{c_b}$ to characterise the wave scale of each breaker analysed. Unsteady aspects of $\boldsymbol{c_b}$ are not considered in P85 in building the $\Lambda(\boldsymbol{c_b})$ distribution, as this relates to the whitecap front behaviour as a spilling plume, not to the scale of the wave that is breaking. Since an active breaker develops on a wave crest which travels at speed c, P85 assumed $c_b = c$, which is taken as the speed at which the whitecap front travels, and determines the breaker scale. This is the c_b adopted by Zappa et al. (2012), Gemmrich et al. (2013), amongst others. However, further refinement is involved in relating c_b to c, as discussed in A.2 below.

SM15a (Section 3) used a different method (Kleiss and Melville, 2011) which bins the time-dependent history of each breaker front according to its *instantaneous* velocity. The instantaneous $\Lambda(c)$ contribution from each breaking front during its active lifetime is distributed to a bandwidth of slower velocity bins, down to O(50%) of its initial velocity. The ensemble of these individual partitionings constitutes their $\Lambda(c)$ spectra. Full details are given in Sutherland and Melville (2013) and its supplementary annexe. Note that this methodology shifts their $\Lambda(c)$ to lower wave speeds, causing a systematic bias of the breaking dissipation rate spectrum to the shorter wave scales. Assuming the linear dispersion relation, this also results in a weighted redistribution of $\Lambda(k)$. The spectral breaking dissipation rate contribution from each breaker is redistributed from its initial breaking wavenumber to shorter scales up to O(4) times its initial wavenumber. Since the speed of the spilling crest front does not directly relate to the speed of each wave that is breaking, this precludes the use of the linear dispersion relation to convert breaker speed to wavenumber. If either $\Lambda(c)$ or $\Lambda(k)$ is used to estimate higher order moments such as S_{ds} via Eq. (4) in SM15a, it also distorts the S_{ds} distribution.

A third method based on whitecap processing in the image spectral (FFT) domain (Thomson and Jessup, 2007) was used by Thomson et al. (2009). While this method significantly reduces data analysis effort, it is also influenced by breaker front slowdown and has windowing issues with aliasing beyond the measured bandwidth (Schwendeman et al., 2014). This method is mentioned for reference only and not investigated here.

A.2. Generic wave crest slowdown

The generic crest speed slowdown mechanism (Banner et al., 2014) clearly affects the initial breaker front speed. Allis (2013, Chapter 7, Fig. 7.10) made frame-by-frame video measurements of breaking wave packets in a wave basin. These show that the leading edge of 2D and 3D spilling breakers initially advances at a mean rate of $[0.87 \pm 0.08]c_0$, where c_0 is the equivalent linear wave speed of the underlying wave. This observed generic breaking front speed of $\sim 0.87c_0$ should be taken into account when assigning the correct wave speed scale c for the $\Lambda(c)$ extracted from video measurements. The observed 13% mean speed reduction requires a 15% increase ($1/0.87 = 1.15$) in the initial speed attributed to a given breaking event to match the linear speed of the underlying wave. This shifts the observed $\Lambda(c)$ distribution towards higher speeds. This is important if the data is transformed to $\Lambda(k)$ distributions for comparison with standard spectral wave model output, as it results in a systematic shift to O(30%) lower wavenumbers.

After applying the generic slowdown correction determined by Allis (2013), we now suppress the b subscript in c_b and adopt c as the appropriate speed-corrected measure of the wave scale, with the corresponding spatial wavenumber k given by the linear dispersion relation.

In summary, in physical space the assignment of speed c to a given breaker is found by tracing the breaking front speed sequence back to the speed of the initial breaking, which is then increased by 15% to account for the generic crest slowdown.

A.3. Impact on $\Lambda(c)$ spectra and resultant breaking dissipation rates

This subsection assesses the impact of the two factors identified in A.1 and A.2 on the $\Lambda(c)$ distributions and on the allied results for spectral breaking dissipation rate contributions, as shown in Fig. 6(a) in Section 3 of SM15a

Our first goal was to reconstruct, as closely as possible, the $\Lambda(c)$ spectra consistent with the P85 framework, hereafter labelled $\Lambda_{\mathrm{BL}}(c)$, denoting Base Line Λ. The Instantaneous Speed Binned (hereafter ISB) transformed $\Lambda(c)$ reported by SM15a, hereafter labelled $\Lambda_{\mathrm{IS}}(c)$, cannot be inverted explicitly, so we applied an iterative ISB transformation to a set of trial Λ_{BL} spectra to emulate the SM15a methodology described above. This Transformed Baseline Λ is labelled $\Lambda_{\mathrm{TB}}(c)$. If the initial guess for the $\Lambda_{\mathrm{BL}}(c)$ is correct, then the $\Lambda_{\mathrm{TB}}(c)$ will closely match the $\Lambda_{\mathrm{IS}}(c)$. The trial spectral function $\Lambda_{\mathrm{BL}}(c)$ before modification by the SM15a ISB process was modelled as having the form:

$$\Lambda_{\mathrm{BL}}(c) = r(c)c^{-\mathrm{n}} \tag{A1}$$

where r is an assumed spectral roll-off function at slow wave speeds and c^{-n} is an assumed power law fall-off that follows the measured overall trend. Forms for r and values for n were refined by successive iteration so that the ISB-transformed $\Lambda_{TB}(c)$ spectra matched as closely as possible the $\Lambda_{IS}(c)$ spectra reported by SM15a derived from their measurements.

For each wave age banded case, we formulated a base $\Lambda_{BL}(c)$ spectral function (corresponding to the P85 framework, as specified above (Eq. (A1)). Based on the measured breaker properties reported in Fig. 13 of Kleiss and Melville (2011), we applied a cosine-weighted spectral function (filter) that redistributes the initial breaker crest speed c_{max} from c_{max} to $0.5c_{max}$, peaking at about $0.75c_{max}$. Our equivalent Λ spectral weighting starts at c_{max} and redistributes the spectral density by a cosine window that varies from 0.5 at c_{max}, to 1 at $0.75c_{max}$ and reduces to 0.5 at $0.5c_{max}$. These weightings were then normalised so that their sum was 1. Applying this window successively to our base spectrum $\Lambda_{BL}(c)$ starting at c_{max} and moving sequentially towards slower speeds reshapes to lower speeds the initial base spectrum $\Lambda_{BL}(c)$ to the transformed baseline spectra $\Lambda_{TB}(c)$ for comparison with the $\Lambda_{IS}(c)$ spectra shown Fig. 6(a) of SM15a. By successive iteration where the exponent n and the parameters in the function r (Eq. (A1)) are tweaked, a close correspondence was achieved between the $\Lambda_{TB}(c)$ and the corresponding $\Lambda_{IS}(c)$ spectrum reported for each different wave age band in SM15a. Other choices of weighting distribution functions that spread the front speed over 0.5 to 1 only marginally altered the result.

Further, from Allis (2013, Ch.7, p.190, below Fig. 7.10), the observed breaker crest front speed $c = |\mathbf{c}|$ is only 0.87 of the actual underlying linear wave speed, and so the c dependence in $\Lambda_{BL}(c)$ needs to be replaced by $c = 1.15c_0$ to match it to the actual wave speed of the underlying wave, as described towards the end of the Overview section above. This speed correction is also applied to the $\Lambda_{BL}(c)$ spectra to produce a speed-corrected baseline spectrum which is referred to as $\Lambda_{BC}(c)$ (for Baseline Corrected). Fig. A1(a) and (b) shows typical examples of the four different spectra $\Lambda_{IS}(c)$, $\Lambda_{BL}(c)$, $\Lambda_{TB}(c)$ and $\Lambda_{BC}(c)$.

Fig. A1(a) and (b) shows that the fit between $\Lambda_{IS}(c)$ and $\Lambda_{TB}(c)$ is good for young seas and for most speeds for the older seas. The noise in the observed $\Lambda_{IS}(c)$ for larger values of c in older seas arises from a combination of low breaking probabilities in the peak region for older seas, and a limited-duration data record in the observations. Also, $\Lambda_{IS}(c)$ shows a significant shift of the spectral peak towards shorter, slower waves relative to the baseline spectrum $\Lambda_{BL}(c)$, and its spectral peak level has increased. This results from the speed-binning of the slowing breaker fronts. For each of these spectra, the spectral fall-off towards faster waves follows the reference c^{-6} dependence predicted by P85. Also note that for all the $\Lambda(c)$, the peak values for the old seas are much lower than for the young seas. Fig. A1(c) and (d) show the fifth moment $c^5\Lambda(c)$ which underpins the breaking dissipation rate (S_{ds}^{br}) (SM15a, Eq. (4)). Their matching plots are shown above in Fig. 10. The c^5 weighting has changed the spectral peak level differential between $\Lambda_{IS}(c)$ and $\Lambda_{BL}(c)$, with the latter now exceeding the former. Note that after speed correction of $\Lambda_{BL}(c)$ to $\Lambda_{BC}(c)$, the difference between $\Lambda_{BC}(c)$ and $\Lambda_{IS}(c)$ is about one order of magnitude for this case.

It is worth noting that the assessment of the contributions of breaking waves travelling in given speed bands depends on the $\Lambda(c)$ processing methodology, as shown in Fig. A1. However, the actual choice of the nominal speed bands, e.g. $c < 1$ m/s for microbreakers, does not depend on the $\Lambda(c)$ processing methodology.

Fig. A1(e) and (f) shows the breaking dissipation rate (S_{ds}^{br}) after multiplication by the breaking strength parameter b used in SM15a, formulated following R12. Here it is seen that breaking waves at the spectral peak of the wave height distribution dominate the breaking dissipation rate (S_{ds}^{br}) for all four $\Lambda(c)$ distributions. The $\Lambda_{BC}(c)$ breaking dissipation rate is higher in the peak region than $\Lambda_{IS}(c)$, but lower for the smaller-scale breakers. This is also true for the old sea case, except spectral peak breaking waves no longer dominate as the older sea peak wave breaking dissipation rates are much lower than for the young seas.

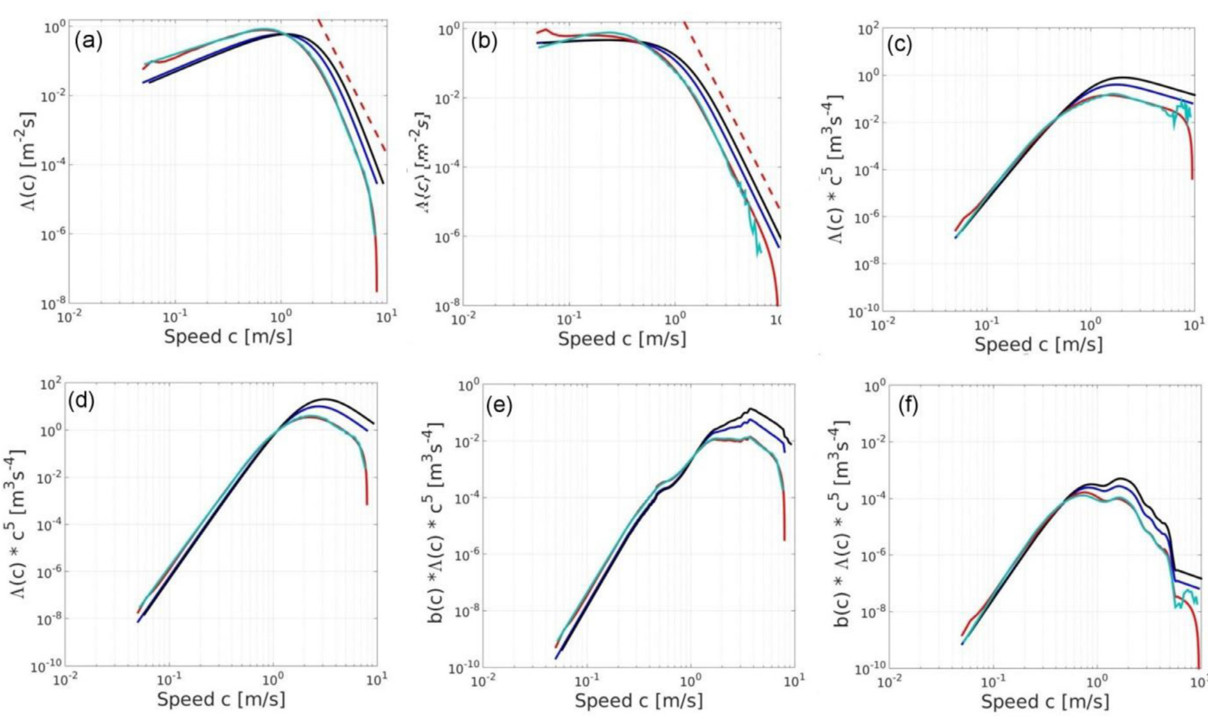

Fig. A1. (a) $\Lambda(c)$ against c for young seas (b) $\Lambda(c)$ against c for old seas. The cyan line is $\Lambda_{IS}(c)$, the blue line is $\Lambda_{BL}(c)$, the red line is $\Lambda_{TB}(c)$ and the black line is $\Lambda_{BC}(c)$. The red dashed line is the P85 c^{-6} dependence. Fig. A1(c) and (d) are the matching plots of $c^5\Lambda(c)$ against c, and Fig. A1(e) and (f) are the matching plots of b (B)$*c^5\Lambda(c)$ against c. Colours are matched in all panels. (For interpretation of the references to colour in this figure legend, the reader is referred to the web version of this article.)

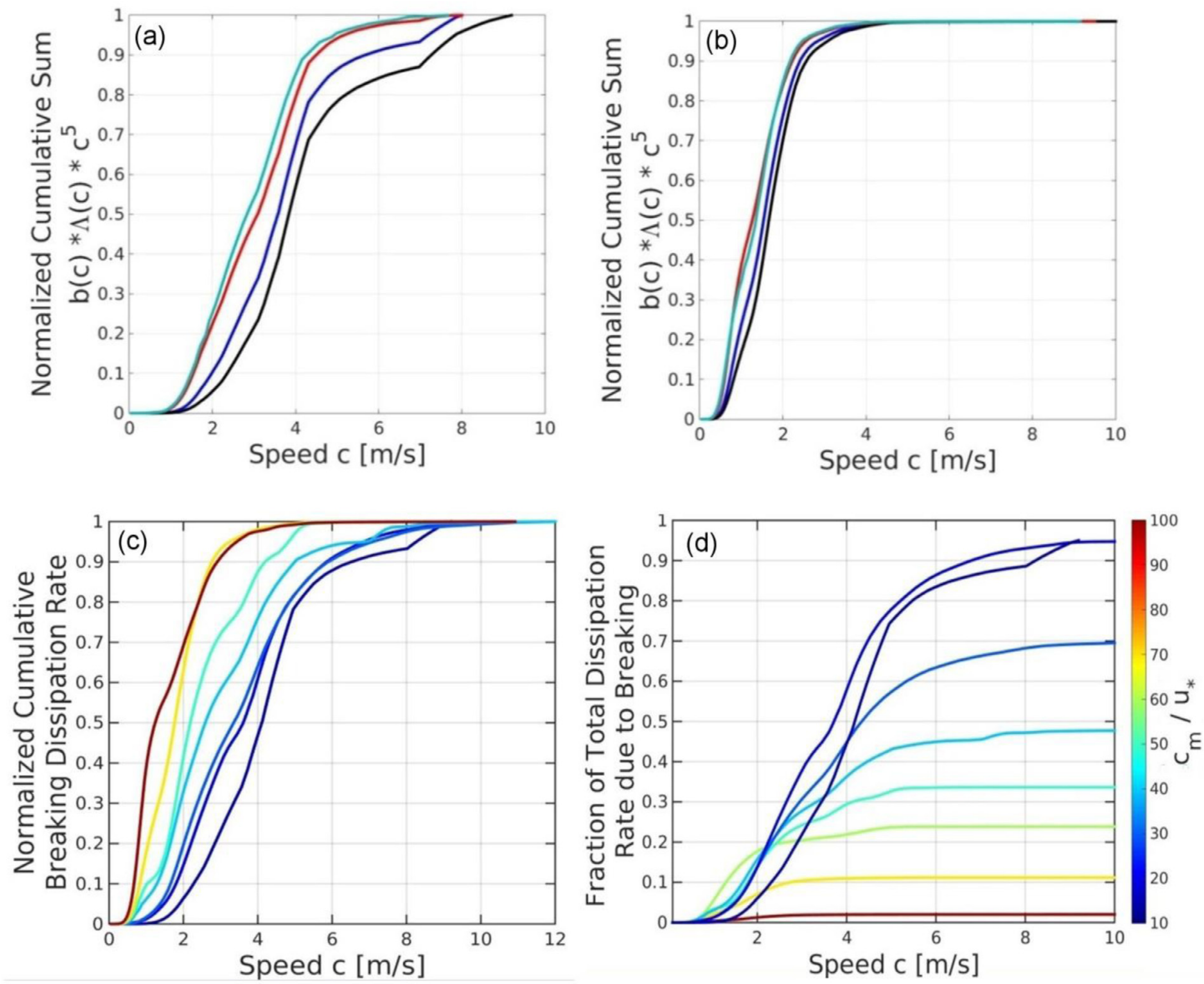

Fig. A2. Normalised cumulative results for the data shown in Fig. A1 for (a) young seas and (b) old seas. Colours match those in Fig. A1. (c) normalised cumulative breaking dissipation rate of based on the speed-corrected baseline spectrum $\Lambda_{BC}(c)$ against breaker front speed for the different binned wave ages, and (d) cumulative breaking dissipation rate of as a fraction of the total wave dissipation rate (S_{ds}), calculated from the speed-corrected baseline spectrum $\Lambda_{BC}(c)$ for breaking fronts with speeds up to speed c, for the range of binned wave age cases reported in SM15a. (For interpretation of the references to colour in this figure legend, the reader is referred to the web version of this article.)

The cumulative breaking dissipation rate of $S_{ds}^{br}(c)$ results from $\Lambda_{IS}(c)$ in Fig. A1(e) and (f) can also be compared by constructing the corresponding normalised cumulative versions of the results. These are plotted in Fig. A2(a) and (b).

For young seas in Fig. A2(a), the cumulative dissipation rate of $S_{ds}^{br}(c)$ from breaking waves travelling at less than 2 m/s is seen to be a small percentage of the total breaking wave dissipation rate (S_{ds}^{br}). Note that the different $\Lambda(c)$ processing methods have a significant affect. For the older wind sea case shown in Fig. A2(b), the breaking waves travelling at speeds less than 2 m/s contribute a large percentage of the total breaking wave dissipation rate (S_{ds}^{br}). It is worth re-emphasising that this is only the dissipation rate from wave breaking, and that for old seas, the dissipation rate from breaking (S_{ds}^{br}) is only a small fraction of the total wave dissipation rate (S_{ds}).

Fig. A2(c) shows the normalised cumulative dissipation rate due only to breaking (S_{ds}^{br}) as a function of mean wave age based on our $\Lambda_{BC}(c)$ spectrum, for comparison with the SM15a results based on their $\Lambda_{IS}(c)$ spectrum shown in Fig. 1 above. The difference between Fig. A2(c) and (d) is that Fig. A2(c) is normalised by the spectrally-integrated dissipation rate due to breaking (S_{ds}^{br}), whereas Fig. A2(d) is normalised by the total wave dissipation rate (S_{ds}) from all sources. For old seas (red line) in Fig. A2(c), the breaking dissipation rate (S_{ds}^{br}) is dominated by waves travelling slower than 2 m/s, but for Fig. A2(d), the breaking dissipation rate (S_{ds}^{br}) is a very small fraction of the total. For younger seas (blue lines), Fig. A2(d) shows that breaking is the dominant form of dissipation, but waves travelling slower than 2 m/s make up, at most, less than 20% of the total wave dissipation rate (S_{ds}) (Fig. A2(d)). These results are summarised in Fig. 7b.

When Fig. 8 based on $\Lambda_{BC}(c)$ is compared with Fig. 7 based on $\Lambda_{IS}(c)$, it is seen that the contributions in Fig. 8 are almost halved relative to Fig. 7. This indicates an even lower contribution of the microbreakers and small whitecaps to the total wave dissipation rate (S_{ds}) in the wave boundary layer.

References

Allis, M.J., 2013. The Speed, Breaking Onset and Energy Dissipation of 3D Deep Water Breaking Waves. PhD thesis. The University of New South Wales Sydney, Australia, pp. 2052.

Banner, M.L., Morison, R.P., 2010. Refined source terms in wind-wave models with explicit wave breaking forecasts. Part I. Model framework and validation against field data. Ocean Modell. 33, 177–189.

Banner, M.L., Barthelemy, X., Fedele, F., Allis, M., Benetazzo, A., Dias, F., Peirson, W.L., 2014. Linking reduced breaking crest speeds to unsteady nonlinear water wave group behavior. Phys. Rev. Lett. 112, 114502.

Cauillez, G., 2011. Wind wave breaking from micro to macroscale. In: Komori, S., McGillis, W., Kurose, R. (Eds.), Gas Transfer at Water Surfaces. Kyoto University Press, pp. 151–163.
Craig, P.D., Banner, M.L., 1994. Modeling wave-enhanced turbulence in the ocean surface layer. J. Phys. Oceanogr. 24, 2546–2559.
Chawla, A., Tolman, H.L., Gerald, V., Spindler, D., Spindler, T., Alves, J.G.M., Cao, D., Hanson, J.L., Devaliere, E.-M., 2013. NCEP NOTES - a multigrid wave forecasting model: a new paradigm in operational wave forecasting. Weather and Forecasting 28, 1057–1078. http://dx.doi.org/10.1175/WAF-D-12-00007.1.
Dimas, A.A, 2007. Large-wave simulation of microscale breaking waves induced by a free-surface drift layer. Wave Motion 44, 355–370.
Frew, N.M., et al., 2004. Air-sea gas transfer: its dependence on wind stress, small-scale roughness, and surface films. J. Geophys. Res. 109, C08S17. http://dx.doi.org/10.1029/2003JC002131.
Gemmrich, J.R., 2010. Strong turbulence in the wave crest region. J. Phys. Oceanogr. 40, 583–595.
Gemmrich, J.R., Zappa, C.J., Banner, M.L., Morison, R.P., 2013. Wave breaking in developing and mature seas. J. Geophys. Res. 118, 4542–4552. http://dx.doi.org/10.1002/jgrc.20334.
Guo, X., Shen, L., 2014. Numerical study of the effect of surface wave on turbulence underneath. Part 2. Eulerian and Lagrangian properties of turbulence kinetic energy. J. Fluid Mech. 744, 250–272.
Jessup, A.T., Zappa, C.J., 1997. Defining and quantifying microscale wave breaking with infrared imagery. J. Geophys. Res. 102 23,145-23,153.
Kleiss, J.M., Melville, W.K., 2011. The analysis of sea surface imagery for whitecap kinematics. J. Atmos. Ocean. Tech. 28, 219–243.
Komen, G.J., Cavaleri, L., Donelan, M.A., Hasselmann, K., Hasselmann, S., Janssen, P.A.E.M., 1994. Dynamics and Modelling of Ocean Waves. Cambridge University Press, Cambridge, pp. 532.
Melville, W.K., 1994. Energy dissipation by breaking waves. J. Phys. Oceanogr. 24, 2041–2049.
Phillips, O.M., 1985. Spectral and statistical properties of the equilibrium range in wind-generated gravity waves. J. Fluid Mech. 156, 505–531.
Phillips, O.M., Banner, M.L., 1974. Wave breaking in the presence of wind drift and swell. J. Fluid Mech. 66, 625–640.
Romero, L., Melville, W.K., Kleiss, J.M., 2012. Spectral energy dissipation due to surface-wave breaking. J. Phys. Oceanogr. http://dx.doi.org/10.1175/JPO-D-1111-1072.1171.
Schwendeman, M., Thomson, J., Gemmrich, J.R., 2014. Wave breaking and dissipation in a young wind sea. J. Phys. Oceanogr 44, 10–127.
Schwendeman, M., Thomson, J., 2015. Observations of whitecap coverage and the relation to wind stress, wave slope, and turbulent dissipation. J. Geophys. Res. http://dx.doi.org/10.1002/2015JC011196.
Siddiqui, M.H.K., Loewen, M.R., 2007. Characteristics of the wind drift layer and microscale breaking waves. J. Fluid Mech. 573, 417–456.
Sullivan, P.P., McWilliams, J.C., 2010. Dynamics of winds and currents coupled to surface waves. Annu. Rev. Fluid Mech. 42, 19–42.
Sutherland, P., Melville, W.K., 2013. Field measurements and scaling of ocean surface wave-breaking statistics. Geophys. Res Lett. 40, 3074–3079.
Sutherland, P., Melville, W.K., 2015a. Field measurements of surface and near-surface turbulence in the presence of breaking waves. J. Phys. Oceanogr. 45, 943–965.
Sutherland, P., Melville, W.K., 2015b. Measuring turbulent kinetic energy dissipation at a wavy sea surface. J. Atmos. Oceanic Technol. 32, 1498–1514.
Terray, E.A., et al., 1996. Estimates of kinetic energy dissipation under surface waves. J. Phys. Oceanogr. 26, 792–807.
Thomson, J., Jessup, A., 2007. A Fourier-based method for the distribution of breaking crests from video observations. J. Atmos. Oceanic Technol. 26, 1663–1671.
Thomson, J., Gemmrich, J.R., Jessup, A.T., 2009. Energy dissipation and the spectral distribution of whitecaps. Geophys. Res. Lett. 35.
Veron, F., 2015. Ocean Spray. Ann. Rev. Fluid Mech. 47, 507–538.
Wang, B., Liao, Q., Xiao, J., Bootsma, H.A., 2013. A free-floating PIV system: Measurements of small-scale turbulence under the wind wave surface. J. Atmos. Oceanic Technol. 30, 1494–1510.
Wang, B., Liao, Q., 2016. Field observations of turbulent dissipation rate profiles immediately below the air-water interface. J. Geophys. Res. Oceans 121, 4377–4391. http://dx.doi.org/10.1002/ 2015JC011512.
Zappa, C.J., McGillis, W.R., Raymond, P.A., Edson, J.B., Hintsa, E.J., Zemmelink, H.J., Dacey, J.W.H., Ho, D.T., 2007. Environmental turbulent mixing controls on air-water gas exchange in marine and aquatic systems. Geophys. Res. Lett. 34, L10601.
Zappa, C.J., Banner, M.L., Gemmrich, J.R., Schultz, H., Morison, R.P., LeBel, D.A., Dickey, T., 2012. An overview of sea state conditions and air-sea fluxes during RaDyO. J. Geophys. Res. 117. http://dx.doi.org/10.1029/211JC007336.
Zappa, C.J., Banner, M.L., Morison, R.P., Brumer, S.E., 2016. On the variation of the effective breaking strength in oceanic sea states. J. Phys. Oceanogr. 46, 2049–2061.